Impact of facility timing and coordination for next-generation gravitational-wave detectors

Classical and Quantum Gravity

PAPER

OPEN ACCESS

RECEIVED
17 October 2025

REVISED
11 March 2026

ACCEPTED FOR PUBLICATION
1 April 2026

PUBLISHED
21 April 2026

Impact of facility timing and coordination for next-generation gravitational-wave detectors

Ssohrab Borhanian[1,2,*], **Arianna Renzini**[1,2,3], **Philippa S Cole**[1,2], **Costantino Pacilio**[1,2], **Michele Mancarella**[4] **and Davide Gerosa**[1,2]

[1] Dipartimento di Fisica 'G. Occhialini', Universitá degli Studi di Milano-Bicocca, Piazza della Scienza 3, 20126 Milano, Italy
[2] INFN, Sezione di Milano-Bicocca, Piazza della Scienza 3, 20126 Milano, Italy
[3] Department of Physics, ETH Zürich, Wolfgang-Pauli-Strasse 27, 8093 Zürich, Switzerland
[4] Aix-Marseille Université, Université de Toulon, CNRS, CPT, Marseille, France
[*] Author to whom any correspondence should be addressed.

E-mail: ssohrab.borhanian@unimib.it

Keywords: gravitational waves, next-generation detectors, timing and delays, Einstein telescope, cosmic explorer, LIGO-India, Fisher information formalism

Abstract

While the Einstein telescope and cosmic explorer proposals for next-generation (XG), ground-based detectors promise vastly improved sensitivities to gravitational-wave signals, only joint observations are expected to enable the full scientific potential of these facilities, making timing and coordination between the efforts crucial to avoid missed opportunities. This study investigates the impact of long-term delays on the scientific capabilities of XG detector networks. We use the Fisher information formalism to simulate the performance of a set of detector networks for large, fiducial populations of binary black holes, binary neutron stars, and primordial black-hole binaries. Bootstrapping the simulated populations, we map the expected observation times required to reach a number of observations fulfilling scientific targets for key sensitivity and localization metrics across various network configurations. We also investigate the sensitivity to stochastic backgrounds. We find that purely sensitivity-driven metrics such as the signal-to-noise ratio are not strongly affected by delays between facilities. This is contrasted by the localization metrics, which are very sensitive to the number of detectors in the network and, by extension, to delayed observation campaigns for a detector. Effectively, delays in one detector behave like network-wide interruptions for the localization metrics for networks consisting of two XG facilities. We examine the impact of a supporting, current-generation detector such as LIGO India operating concurrently with XG facilities and find such an addition will greatly mitigate the negative effects of delays for localization metrics, with important consequences on multi-messenger science and stochastic searches.

1. Introduction

Gravitational-wave (GW) astronomy currently relies on four ground-based detector facilities: the LIGO detectors [1] in Hanford, Washington, USA and Livingston, Louisiana, USA, the Virgo detector [2] in Cascina, Italy, and the KAGRA detector [3] in Hida, Japan. A third LIGO detector [4] is under construction in Aundha, Maharashtra, India, adding the fifth and final piece to the global network of second-generation, ground-based detectors. The LIGO, Virgo, and KAGRA detectors observed about 218 compact binary coalescence candidates, including binary black holes (BBHs), binary neutron stars (BNSs), and neutron star-black hole mergers [5–8] during their first three observing runs and the initial part of the fourth run, O4a. Additional data releases for the subsequent parts will follow.

Amidst the excitement of the early years of GW astronomy the community has started to plan for potential upgrades to existing facilities, such as the proposed upgrade to the LIGO detectors from A+ to A# sensitivity [9, 10], in addition to proposals for next-generation (XG), ground-based GW detectors.

Two proposals are currently gathering the most attention: the Einstein Telescope (ET) [11, 12] and cosmic explorer (CE) [13]. Both proposed XG facilities are expected to dramatically improve the GW sensitivity across the audio band ranging from a few to order a thousand Hz, enabling the observation of hundreds of thousands of BBH and BNS signals per year and at much higher fidelities [14–22].

Both proposing teams are still narrowing down the exact configurations of the detector facilities. There are several options under consideration for ET [12, 23] including one triangular configuration with interferometer arm lengths of 10 km in either Sardinia, Italy, or the Meuse-Rhine region between the Netherlands, Belgium, and Germany, as well as two L-shaped configurations with varying arm lengths at both of the aforementioned sites[5]. Similarly, a range of CE [24, 25] configurations are being explored which are centered around one or two L-shaped interferometers with arm lengths of 20–40 km that could be built in the United States and/or Australia.

XG GW detectors require substantial investment and would stand among the foremost frontier science facilities of the coming decades. Therefore, coordination between efforts such as ET and CE will be crucial to maximize their scientific return. Conversely, non-optimal synchronization could represent a major missed opportunity for both astrophysics and fundamental physics. This study aims to investigate the impact of facility timing—such as planning and construction delays—on the scientific capabilities of XG detector networks, focusing on the expected observation times for key metrics in GW astronomy. In particular, some science targets can be achieved relatively quickly by a single XG facility, potentially affecting the scientific rationale for the other facility if it is delayed. Conversely, while other science goals can be reached orders of magnitude faster only if both the ET and CE facilities operate concurrently. In the latter case, the still-under-construction LIGO-India detector can play a crucial role to mitigate the studied delays when operating in tandem with future XG networks [26, 27].

Section 2 describes the science metrics used in this study, the XG networks investigated, and the specifics of the simulated sources. Section 3 presents the impact of XG facility timing on their scientific return, the impact of LIGO-India, the discernability of primordial origin, and the sensitivity to stochastic backgrounds. Finally, Section 4 summarizes and discusses the findings, implications, and caveats of this study.

2. Setup

2.1. Targeted metrics

This study aims to map expectations for observation times required to achieve targeted thresholds for key science metrics in GW astronomy such as signal-to-noise ratio (SNR) and the estimation fidelity in luminosity distance, sky position, and 3D localization; particularly taking into account that detector facilities in networks could commence observation with *delays* with respect to each other. A variety of XG detector networks are examined, as well as three types of compact-binary GW sources, namely BBHs and BNSs of stellar origin and primordial black hole (PBH) binaries of cosmological origin.

The quantities of interest are the expected observation times $T_{\rm obs}$ to reach a number of events $N_{\rm th}$ satisfying the targeted thresholds for nine key science metrics:

(i) full-signal SNR $\rho_{\rm th}$,

(ii) post-merger SNR $\rho_{\rm pm,th}$ (for BBHs),

(iii) early-warning SNR $\rho_{\rm ew,th}$ (for BNSs),

(iv) 90%-credible sky area $\Omega_{\rm th}$,

(v) 90%-credible sky area from early warnings $\Omega_{\rm ew,th}$ (for BNSs),

(vi) relative luminosity distance error $(\Delta D_{\rm L}/D_{\rm L})_{\rm th}$,

(vii) comoving error volume $V_{\rm th}$,

(viii) lower redshift error bound $\Delta z_{\vee,\rm th}$ (for PBH binaries),

(ix) power-law sensitivity $\mathcal{P}_{\mathcal{I}}$ of a set of detectors $\mathcal{I}$ to a stochastic signal.

[5] Recently, a third candidate site in Saxony (Germany) has also been under active consideration, but it is not further investigated in this study, in line with [23].

These metrics are designed to span the full breadth of GW science, from compact-binary astrophysics to multi-messenger studies and tests of General Relativity. In particular, the BBH post-merger regime is defined, for the purposes of this study, to start at a frequency $f_{\rm pm}$ corresponding to the peak of the GW strain in the frequency domain such that

$$\left(\left|\tilde{h}_+ - \mathrm{i}\tilde{h}_\times\right| f^{7/6}\right)_{f=f_{\rm pm}} = \max_f \left[\left|\tilde{h}_+ - \mathrm{i}\tilde{h}_\times\right| f^{7/6}\right], \tag{1}$$

where $h_+, h_\times$ are the Fourier transforms of the plus and cross polarizations of the GW strain. For BNS, the early-warning time is set to $\tau_{\rm ew} = 2\,\mathrm{min}$ before coalescence at which the signal has reached a frequency

$$f_{\rm ew} = 22.2 \times \left(\frac{0.25}{\eta}\right)^{3/8} \left(\frac{2.8 M_\odot}{M}\right)^{5/8} \left(\frac{120\,\mathrm{s}}{\tau_{\rm ew}}\right)^{3/8} \mathrm{Hz}, \tag{2}$$

with symmetric mass ratio $\eta = m_1 m_2/M^2$ and total detector-frame mass of the system $M = m_1 + m_2$. The comoving error volume is computed from the sky area Ω and luminosity distance error $\Delta D_{\rm L}$ as

$$V = \Omega \int_{\Delta z_\vee}^{\Delta z^\wedge} \mathcal{V}_{\rm c}(z)\,\mathrm{d}z, \tag{3}$$

where the differential comoving volume $\mathcal{V}_{\rm c}\,[\mathrm{Mpc}^3\,\mathrm{rad}^2]$ as well as the lower and upper redshift error bounds $\Delta z_\vee = z[D_{\rm L} - \Delta D_{\rm L}]$ and $\Delta z^\wedge = z[D_{\rm L} + \Delta D_{\rm L}]$ are computed using the `Planck18` cosmology [28] with redshift $z[\cdot]$ as a function of luminosity distance.

The metrics (i)–(viii) are computed for 10^6 simulated BBH, BNS, and PBH binary signals using the open-soure Python package `gwbench` [29] which implements the Fisher-matrix formalism [30–32]. The formalism is well-established in GW astronomy for the purposes of benckmarking the science capabilties of XG GW detectors for a large number of signals [16–18, 21, 33] as it provides a fast, efficient resource to compute estimates for parameter errors without the need for full Bayesian parameter estimation. For a comprehensive overview of the caveats and limitations of the Fisher-matrix formalism see [34].

A fiducial, easily rescalable cosmic merger rate $\mathcal{R}$ of $10^5\,\mathrm{yr}^{-1}$, chosen in agreement with the current BBH and BNS estimates from LIGO/Virgo/KAGRA [35], is used to compute the expected observation time $T_{\rm obs}$ for a tuple $(N_{\rm th}, X_{\rm th})$ under the assumption that the mergers are Poisson-distributed in time; $X_{\rm th}$ represents a threshold in one of the key metrics. The computation of the observation time is further bootstrapped 100-fold [36] over a 3-year period to mitigate finite-sampling effects from the set of simulated binary merger; median values are reported throughout this study. Statements on observation times beyond 3 yr are extrapolated and only reported up to 5 yr. The PBH binary merger rate was set to $2 \times 10^6\,\mathrm{yr}^{-1}$ consistent with the population model described below.

Sensitivity of the XG network to stochastic signals, such as the GW background (GWB) from the compact binary populations presented here, is assessed by computing power-law integrated sensitivity curves (PI curves) [37]. A PI curve is the locus where an envelope of stochastic signals each described via a power-law model with a distinct index is tangent to the detector sensitivity, assuming a certain detection statistic threshold (i.e. SNR $\rho = 3$). In practice, this translates to the collection of points at which the tangent power-law stochastic signal would satisfy a given ρ. The ρ statistic used here is defined for two detectors, I and J, assuming joint observing time $T_{\rm obs}$, as [37]

$$\rho_{IJ} = \sqrt{2\,T_{\rm obs}} \left[\int \mathrm{d}f\, \frac{\gamma_{IJ}^2(f) S_{\rm h}^2(f)}{S_{\rm n}^I(f) S_{\rm n}^J((f)}\right]^{1/2}, \tag{4}$$

where γ_{IJ} is the overlap reduction function [38] for the two detectors, which quantifies the decoherence between the two detector sites and orientations, while $S_{\rm h}(f)$ and $S_{\rm n}(f)$ represent the GW power spectral density of the stochastic background and noise power spectral density of each detector, respectively. The GWB SNR ρ_{IJ} scales with the square root of the observing time.

2.2. Sources

The 10^6 signals of all binary populations are generated using the frequency-domain waveform models `IMRPhenomXHM` [39, 40] for BBHs and PBH binaries and `IMRPhenomXAS_NRTidalv2` [41] for BNS. The lower frequency cutoff is set to $f_{\rm l} = 2\,\mathrm{Hz}$ for the ET detectors, $f_{\rm l} = 3\,\mathrm{Hz}$ for LIGO-India, and $f_{\rm l} = 5\,\mathrm{Hz}$ for CE, while the upper frequency cutoff is set to $f_{\rm u} = \min\{1024\,\mathrm{Hz}, 8 f_{\rm isco} = 8\,(6^{3/2}\pi\, GM/c^3)^{-1}\}$ for

all detectors (where G is Newton's constant and c is the speed of light). The frequency step size is set to $\Delta f = 2^{-4}$ Hz. The GW signal model parameters consist of detector-frame chirp mass $M_c = \eta^{3/5} M$, symmetric mass ratio η, spin parameter vectors $\vec{\chi}_1, \vec{\chi}_2$, luminosity distance D_L, time t_c and phase ϕ_c of coalescence, inclination angle ι, right ascension α, declination δ, and polarization angle ψ, as well as the tidal deformability parameters Λ_1 and Λ_2 for BNSs.

The BBH and BNS redshift distributions follow the merger rate density for field BBHs from [42] with $z \in [0, 10]$; for BNS, the Madau–Dickinson [43] star formation rate with $z \in [0, 5]$ is assumed, neglecting metallicity effects; more details on both poulations, e.g. the applied time delay distributions, are reported in [16]. The BBH source-frame masses are distributed according to the median Power-Law+Peak model from the Third GW Transient Catalog [44], while the BNS source-frame component masses follow a Gaussian distribution $\mathcal{N}(\mu = 1.35, \sigma = 0.15)$ constrained within $[1, 2] M_\odot$. The tidal deformability of the component neutron stars is computed from their masses for the `SLY` equation of state [45] as implemented in `bilby` [46]. The component spins are chosen to be aligned with the orbital angular momentum of the binary system with uniformly distributed projections, $\chi_{i,z}^{\rm BBH} \in [-0.75, 0.75]$ and $\chi_{i,z}^{\rm BNS} \in [-0.05, 0.05]$, with $i = 1, 2$. The luminosity distance D_L is calculated from the sampled redshifts using the `Planck18` cosmology [28] while both the time and phase of coalescence are set to $t_c = \phi_c = 0$ for all signals. The sampling method for the four angular parameters is the same for both populations with $\cos(\iota)$, $\cos(\pi/2 - \delta)$ uniformly distributed in $[-1, 1]$ and α, ψ uniformly distributed in $[0, 2\pi]$.

Further, a speculative population of stellar-mass PBHs is studied which may have formed in the very early Universe from, for example, the collapse of large amplitude density perturbations (see e.g. [47–49] for recent reviews). If such a population exists, since they would have populated the Universe long before matter-radiation equality and only interact gravitationally, they would automatically explain some fraction of the dark matter energy density budget. Their abundance, usually quantified by $f_{\rm PBH} = \Omega_{\rm PBH}/\Omega_{\rm CDM} \leqslant 1$, is the fraction of the dark matter energy density today $\Omega_{\rm CDM}$ that is contained within PBHs. In the stellar-mass range, GW observations place some of the most stringent constraints on their abundance such that $f_{\rm PBH} \lesssim 10^{-3}$ [50]. While initial PBH clustering is expected to have a negligible impact on this mass range [51], extended mass distributions may relax the constraints [52]. However, even the detection of a single PBH binary would be extremely powerful for narrowing down our theories of the early Universe [53], as well as explaining a fraction of the dark matter. XG GW detectors open up the possibility of detecting very high redshift BBH mergers, which would provide smoking gun evidence of a primordial origin [54–56].

Assuming a log-normal probability density function for the mass distribution of PBHs,

$$\psi(m) = \frac{1}{m\sigma\sqrt{2\pi}} \exp\left\{ -\frac{\left[\log(m/m_c) + 0.5\sigma^2\right]^2}{2\sigma^2} \right\} \tag{5}$$

centred on PBH mass $m_c = 50 M_\odot$ with width $\sigma = 0.7$, the differential merger rate is calculated as [57]

$$\mathrm{d}R(m_1, m_2, z) = \frac{1.6 \times 10^6}{\mathrm{Gpc}^3\,\mathrm{yr}} f_{\rm sup} f_{\rm PBH}^{53/37} \left(\frac{m_1 m_2}{M^2}\right)^{-34/37} M^{-32/37} \psi(m_1)\,\psi(m_2)\,(1+z)^{\alpha}\,\mathrm{d}m_1\,\mathrm{d}m_2, \tag{6}$$

where $f_{\rm sup}$ is a suppression factor that quantifies the disruption of binaries due to smaller PBHs before they merge. The fraction $f_{\rm PBH} = 1.2 \times 10^{-3}$ and the values of m_c and σ in the mass distribution are taken so as to conservatively respect current observational constraints. The redshift dependence is parametrized by a power-law where $\alpha = 1.28$ represents a PBH population which is Poisson distributed [57–60]. To obtain binary PBH source population, the binary component masses m_1, m_2 and the redshift z are sampled from the differential merger rate between $1 - 100\,\mathrm{M}_\odot$ and $1 - 100$, respectively, with fixed $f_{\rm sup} = 1$. All population-level results for $f_{\rm sup} = 10^{-3}$ are obtained by rescaling the results of this population.

Finally, the GWB signal is computed for all of the simulated source populations. The adimensional spectral energy density $\Omega_{\rm GWB}(f) = \rho_c^{-1}\,\mathrm{d}\rho/\mathrm{d}\ln f$ is employed, in line with similar works in the literature that aim to assess sensitivity to compact binary backgrounds [23, 61–65]. The spectrum for compact binaries is defined as [66]

$$\Omega_{\rm GWB}^{\rm CBC}(f) = \frac{f}{\rho_c} \int \mathrm{d}z \frac{R(z)}{(1+z)H(z)} \left\langle \left.\frac{\mathrm{d}E_s}{\mathrm{d}f_s}\right|_{f_s} \right\rangle, \tag{7}$$

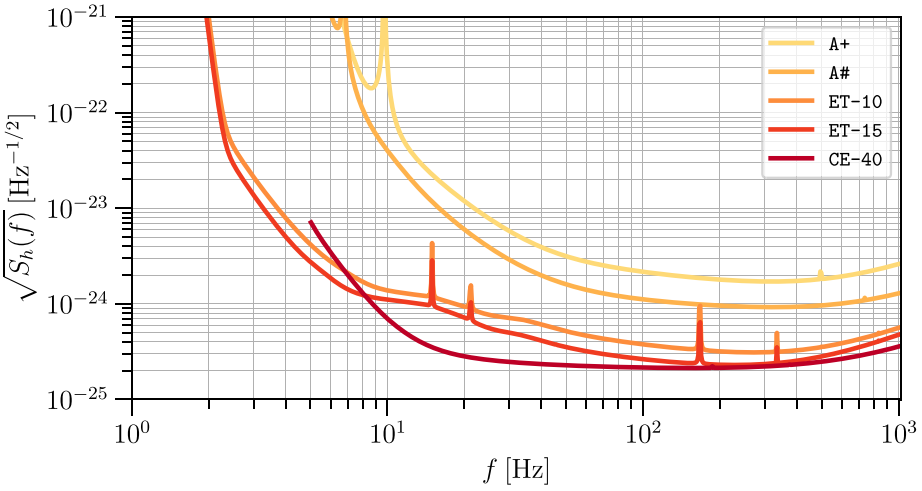

Figure 1. Detector sensitivity curves used in this study, see section 2.3. The `A+` and `A#` curves are used for the LIGO-India detector `I`, `ET-10` and `ET-15` for ET configurations `ET-`△ and `ET-2L`, respectively, and `CE-40` for the CE facility `CE`.

where $R(z)$ is the source-frame merger rate per comoving volume and $\mathrm{d}E_\mathrm{s}/\mathrm{d}f_\mathrm{s}$ is the binary source-frame energy spectrum, while ρ_c is the critical energy density of the Universe, and $H(z)$ is the Hubble parameter at redshift z. The angle brackets indicate an ensemble average over the population considered, which is performed here using the `popstock` [64] code.

2.3. Detector networks

This study considers 15 different XG detector networks, consisting of five XG facility configurations, namely `ET-`△, `ET-2L`, `CE`, `ET-`△ + `CE`, and `ET-2L` + `CE`, which are studied in isolation or in tandem with one of two LIGO-India configurations, `I+` and `I#`, using the A+ or A# detector sensitivities, respectively. The adopted detector sensitivity curves are shown in figure 1 and crucially all detectors are assumed to operate immediately at their respective design sensitivity. The detector configurations are specified in appendix A. The following labels are used throughout this study to refer to the networks, detectors, and sensitivities:

- `ET-`△: single 10 km, triangular interferometer at fiducial ET site in Sardinia, Italy [12], with `ET-10` (10 km-xylophone) sensitivity curve in `ET10kmcolumns.txt` from [67] for each of the three sub-interferometer;
- `ET-2L`: two 15 km, L-shaped interferometers at fiducial ET sites in Sardinia, Italy and in the Meuse-Rhine region between the Netherlands, Belgium, and Germany [12], with `ET-15` (15 km-xylophone) sensitivity curve in `ET15kmcolumns.txt` from [68] for both interferometers, the two detectors are rotated by 45° with respect to each other;
- `CE`: single 40 km, L-shaped interferometer at fiducial CE site in Idaho, USA [13], with `CE-40` sensitivity curve in `cosmic_explorer_40km.txt` from [69];
- `I+` and `I#`: single 4 km, L-shaped interferometer at the LIGO-India site in Maharashtra, India [4], with `A+` sensitivity curve in `aplus.txt` from [70] or `A#` sensitivity curve in `asharp_strain.txt` from [71], respectively;

While this investigation focuses on LIGO-India, any other current-generation detector—namely LIGO-Hanford, LIGO-Livingston, Virgo, or KAGRA—would have a similar impact [26] if operated at the studied sensitivities in tandem with XG detectors. Regardless, with LIGO-India under active construction and targeting observations to commence in 2030, this facility presents a natural choice for this study.

3. Results

3.1. XG timing

To investigate the impact of timing and coordination of XG detector facilities, particularly the potential for delays in observation campaigns, figure 2 compares the expected observation times T_obs to detect

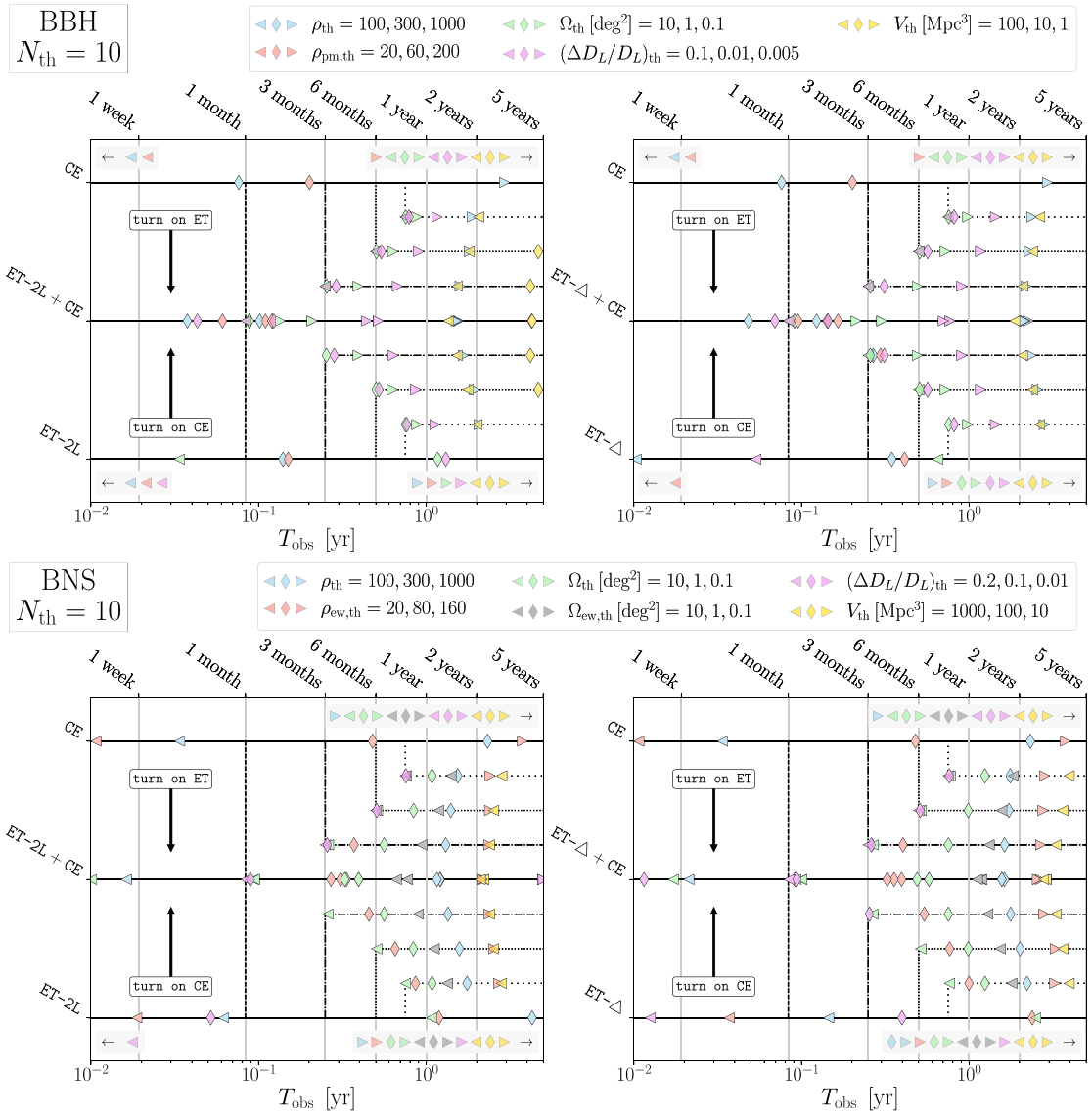

Figure 2. Comparison of the expected observation times $T_{\rm obs}$ to reach a target of $N_{\rm th} = 10$ BBH (top) and BNS (bottom) signals satisfying three different thresholds for SNR $\rho_{\rm th}$, sky area $\Omega_{\rm th}$, relative luminosity distance error $(\Delta D_{\rm L}/D_{\rm L})_{\rm th}$, comoving error volume $V_{\rm th}$, post-merger SNR $\rho_{\rm pm,th}$, early-warning SNR $\rho_{\rm ew,th}$, and sky area $\Omega_{\rm ew,th}$. For each of these, three thresholds are considered and indicated with different marker shapes. The solid, horizontal lines represent the timelines for the base detectors (CE atop and ET beneath) and the combined network (center) to reach the targets; in addition to the impact of potential observation delays of 1 (dashed), 3 (dashed-dotted), 6 (dotted), and 9 (loosely dotted) months. Targets that are either completed within 0.01 yr or that cannot be reached within 5 yr are places in gray boxes. For example, a single L-shaped `CE` detector would not be able to detect $N_{\rm th} = 10$ BBHs to within $\Omega_{\rm th} = 10\,\rm deg^2$ (◀, top left panel) within 5 yr, while `ET-2L` and the joint network `ET-2L` + `CE` would reach this target within two weeks or less than 0.01 yr, respectively.

$N_{\rm th} = 10$ BBH and BNS signals for metrics of interest (i) - (vii) at three target thresholds for the five studied XG facility configurations of ET and CE, `ET-`△, `ET-2L`, `CE`, `ET-`△ + `CE`, and `ET-2L` + `CE`. In particular, it illustrates the impact of either of the base XG facilities experiencing long-term delays of $\tau_{\rm delay} = 1, 3, 6, 9$ months within a three-year-long observation campaign. Appendix B presents the respective values of the plotted observation times. Metrics will be neglected in the discussion below if all networks require observation times $T_{\rm obs} \gtrsim 5\,\rm yr$ to reach the targeted thresholds, as potential errors in the extrapolation of the observation time beyond 5 years would make these results unreliable. Appendix C presents more complete maps of expected observation times $T_{\rm obs}$ over $N_{\rm th} \in [1, 100]$ for a wide range of targeted thresholds in the key metrics of interest in this study.

Figure 2 presents the expected observation times $T_{\rm obs}$ as markers along horizontal lines which represent different detector and network configurations: solid lines signify the base XG configurations, `ET-`△, `ET-2L`, `CE`, and the two networks, `ET-`△ + `CE` and `ET-2L` + `CE`, combining the ET configurations with CE. Non-solid lines indicate the observation scenarios in which one of the base XG facilities experiences long-term delays of $\tau_{\rm delay} = 1, 3, 6, 9$ months ahead of their observation campaign. The marker colors and

shapes indicate the metrics of interest and three different target thresholds, respectively. In particular, each non-solid line begins at a specific time from either the top (CE) or bottom (ET) solid line in each panel, indicating the time CE or ET operates by themselves, before the other facility turns on after the delay. Conversely markers will not be present along the non-solid lines if the respective base XG facility reaches the targeted threshold before the other facility turns on.

The SNR metrics—full signal, BBH post-merger, and BNS early-warning—are the least sensitive in observation time to such delays and adhere to the most sensitive, operating GW detector facility since SNRs add as sum of squares. All base XG configurations observe the targeted number of $N_{\rm th} = 10$ signals satisfying ${\rho_{\rm th}}^{\rm BBH} = 100$, ${\rho_{\rm pm,th}}^{\rm BBH} = 20$, ${\rho_{\rm th}}^{\rm BNS} = 50$, and ${\rho_{\rm ew,th}}^{\rm BNS} = 20$ within one month, with ET-△ requiring two for ${\rho_{\rm th}}^{\rm BNS} = 50$. Thus, months-long observation delays will not affect the realization of these targets; at least in a significant way. This statement holds for BBHs observed with CE and ET-2L as well, albeit in a weaker sense, for the higher SNR thresholds of ${\rho_{\rm th}}^{\rm BBH} = 300$ and ${\rho_{\rm pm,th}}^{\rm BBH} = 60$: both networks require less than three months of observation time to reach the target; ET-△ would require up to five months. The largest impact is seen for the small populations of high-SNR events (${\rho_{\rm th}}^{\rm BBH} = 1000$, ${\rho_{\rm pm,th}}^{\rm BBH} = 200$, ${\rho_{\rm th}}^{\rm BNS} = 200$, and ${\rho_{\rm ew,th}}^{\rm BNS} = 160$) which require $T_{\rm obs} \gtrsim 3\,{\rm yr}$ in all shown XG networks. The addition of the second XG facility after $\tau_{\rm delay} = 0.75\,{\rm yr}$ results in the smallest relative speed-ups for the observation time which vary across the these high-SNR events in the following ranges: $5.3 - 24\times$ for ET-△, $2.9 - 5.5\times$ for ET-2L, and $1.2 - 1.6\times$ for CE.

The localization metrics—sky area, relative luminosity distance error, and comoving error volume—are very sensitive to the number of detectors, particularly at non-colocated sites, in the network. Hence, both ET-△ (effectively two colocated detectors) and ET-2L (two non-colocated detectors) outperform the more sensitive, one-detector facility of CE for these metrics: CE alone cannot achieve any of the target localizations in $\Omega_{\rm th}$ and $(\Delta D_{\rm L}/D_{\rm L})_{\rm th}$ within 5 years, see also appendix C, while ET-2L (ET-△) will see BBH and BNS signals with ${\Omega_{\rm th}}^{\rm BBH} = 10\,{\rm deg}^2$, ${(\Delta D_{\rm L}/D_{\rm L})_{\rm th}}^{\rm BBH} = 0.1$, ${\Omega_{\rm th}}^{\rm BNS} = 10\,{\rm deg}^2$, and ${(\Delta D_{\rm L}/D_{\rm L})_{\rm th}}^{\rm BNS} = 0.1$ approximately ten times every 2 weeks (8 months), 16 h (3 weeks), 1.1 years (2.5 years), and 3 weeks (5 months), respectively. This is in line with previous studies that underlined how a single XG interferometer alone would not meet many science requirements [12, 23]. The two-facility networks, ET-△ + CE and ET-2L + CE, speed up the observation times by one to three orders of magnitude, decreasing the observation times for the aforementioned metrics to approximately few hours, few hours, less than a week, and few days, respectively. In fact, in comparison to the one-facility configurations, these networks will observe the target of 10 BBH and BNS signals satisfying any of the investigated sky and distance localization metrics so rapidly that the resulting observation times are fully governed by the raw, short observation time of the two-facility network in addition to whatever delays are present in their component facilities; in other words, observation delays are essentially equivalent to network-wide interruptions for achieving the studied targets for the localization metrics. This statement softens as the targeted number of signals $N_{\rm th}$ becomes of order unity, as statistical fluctuations become more relevant.

The early-warning sky area $\Omega_{\rm ew,th}$ for BNSs and comoving volume error $V_{\rm th}$, are particularly poorly constrained. The single-facility configurations, even ET-2L with its two non-colocated detectors, are unable to observe $N_{\rm th} = 10$ BBH and BNS signals satisfying any of the targeted thresholds for $\Omega_{\rm ew,th}$ and $V_{\rm th}$ within 5 years while the two-facility networks achieve the targets, ${\Omega_{\rm ew,th}}^{\rm BNS} = 10\,{\rm deg}^2$, ${V_{\rm th}}^{\rm BBH} = 100\,(10)\,{\rm Mpc}^3$, and ${V_{\rm th}}^{\rm BNS} = 1000\,{\rm Mpc}^3$, within 0.66–1.1 years, 1.4 – 1.9 (4.3 with ET-2L + CE) years and 2.1–2.8 years, respectively. Again, delays in the observation times are effectively equivalent to extensions of the observation campaign.

3.2. Impact of LIGO-india

Figure 3 shows the impact of LIGO-India, in I+ or I# configuration, when operating in tandem with the five aforementioned XG networks, ET-△, ET-2L, CE, ET-△ + CE, and ET-2L + CE. The respective data is collected across tables B1, B2, and B3. The addition of LIGO-India, even in the more sensitive A# configuration, has a negligible effect on the expected observation times $T_{\rm obs}$ to reach the targeted thresholds for the SNR metrics which are dominated by the more sensitive XG detectors in the network (see [26] for a previous investigation). The same applies to the early-warning sky area $\Omega_{\rm ew,th}$ for BNS signals.

The other localization metrics paint the opposite picture: the addition of LIGO-India dramatically decreases the observation times for the these metrics in the single-facility configurations, ET-△, ET-2L, and CE. Both BBH and BNS signals see one to two orders of magnitude speed-ups in the observation times to achieve the targets for the sky area and luminosity distance error metrics. In both cases, the A# configuration roughly halves the observation times compared to the I+ configuration. The impact is expectedly less severe for the two-facility networks, ET-△ + CE and ET-2L + CE, and of the order of

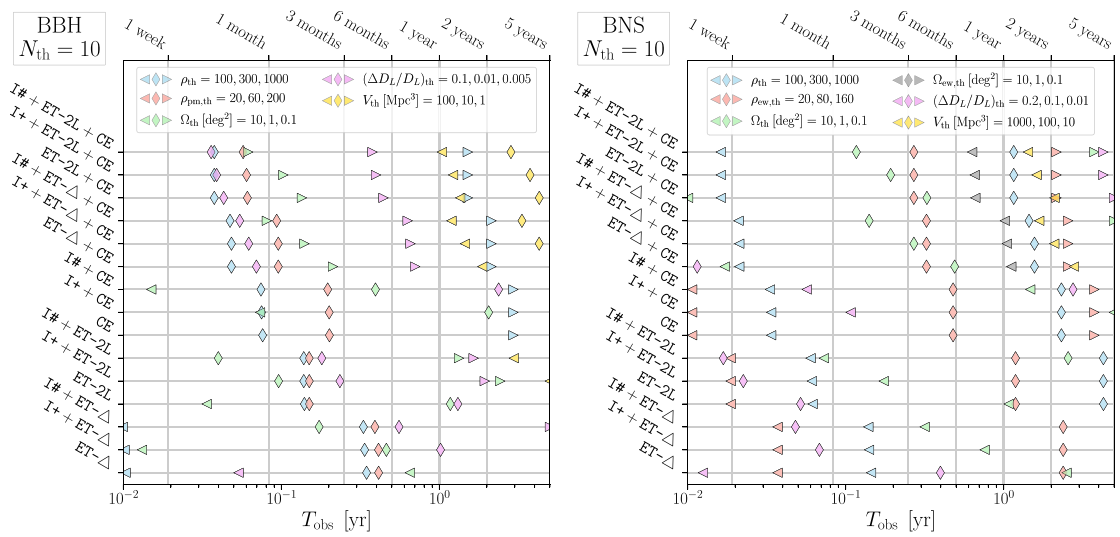

Figure 3. Impact of the addition of LIGO-India, either in `I+` or `I#` configuration, to five XG detectors and networks, `ET-△`, `ET-2L`, `CE`, `ET-△ + CE`, `ET-2L + CE`, on the expected observation times $T_{\rm obs}$ to reach a target of $N_{\rm th} = 10$ BBH (left) and BNS (right) signals satisfying three different thresholds for SNR $\rho_{\rm th}$, sky area $\Omega_{\rm th}$, relative luminosity distance error $(\Delta D_{\rm L}/D_{\rm L})_{\rm th}$, or comoving error volume $V_{\rm th}$ in addition to post-merger SNR $\rho_{\rm pm,th}$ for the BBHs and early-warning SNR $\rho_{\rm ew,th}$ and sky area $\Omega_{\rm ew,th}$ for the BNSs.

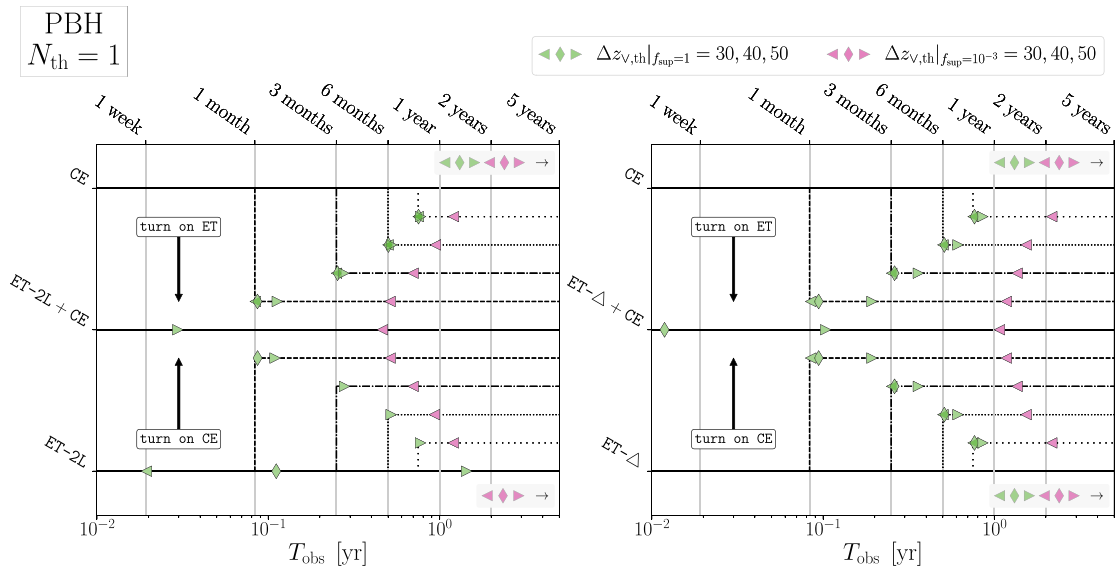

Figure 4. Comparison of the expected observation times $T_{\rm obs}$ to reach a target of $N_{\rm th} = 1$ PBH signal satisfying three different thresholds for the lower redshift error bound $\Delta z_{{\rm V},{\rm th}} \in \{30, 40, 50\}$ at two values for the PBH-formation suppression factor $f_{\rm sup} \in \{10^{-3}, 1\}$ when observed by the three base XG facility configurations, `ET-△` (right), `ET-2L` (left), `CE` (both), and two networks, `ET-△ + CE`, `ET-2L + CE`, combining the ET configurations with CE. The solid, horizontal lines represent the timelines for the base detectors (CE atop and ET beneath) and the combined network (center) to reach the targets. The non-solid lines take potential observation delays of 1 (dashed), 3 (dashed-dotted), 6 (dotted), and 9 (loosely dotted) months in either base detector into account, with the respective non-solid, vertical lines indicating the end of the delay. Gray boxes indicate—for each base detector—the targets that either are completed within 0.01 year or that cannot be reached within 5 yr.

10-140% for BBH and 10%-250% for BNS signals. Hence, the impact of a current-generation detector operating in tandem with an XG network is *not* negligible in the context of reaching the investigated science goals, particularly when potential delays in the observation time of XG facilities are considered.

3.3. Discernability of coalescences of PBHs

The redshift at which stellar-mass BBHs merge is one of the key indicators to discern primordial from astrophysical-origin BBHs [72], as the latter are not expected to merge at redshifts $z \gtrsim 30$ [73, 74]. Hence, figure 4 presents the expected observation times $T_{\rm obs}$ for detecting at least $N_{\rm th} = 1$ PBH signal

satisfying $\Delta z_{\vee,\mathrm{th}} = 30, 40, 50$ for the lower redshift error bounds at two values for the suppression factor $f_{\mathrm{sup}} = \{10^{-3}, 1\}$, which captures our uncertainty on how many PBHs that form binaries in the early Universe are disrupted before merging. In the pessimistic scenario of $f_{\mathrm{sup}} = 10^{-3}$, none of the base XG detector facilities, ET-△, ET-2L, and CE, will be capable of observing even a single PBH signal to be from $\Delta z_{\vee,\mathrm{th}} \geqslant 30$ within 5 year, requiring joint observation of this population with the ET-CE networks, ET-△ + CE and ET-2L + CE. Excitingly, the results show that with both XG detectors online, a single PBH binary with redshift $\Delta z_{\vee,\mathrm{th}} \geqslant 30$ will be detectable within 6 months in ET-2L + CE and within a year in ET-△ + CE. Therefore, any delay in the observation campaign of either ET or CE would directly translate to an equal delay in achieving a confident detection of a PBH binary based on redshift measurements alone. Even at $f_{\mathrm{sup}} = 1$, only the two-detector facility ET-2L would be capable of discerning, almost once a week, if a BBH is merging at redshift $z \geqslant 30$, and thus of primordial origin (see also [12] for similar conclusions). Figure C3 in appendix C shows that LIGO-India in A# configuration would enable the triangular ET configuration ET-△ to observe $N_{\mathrm{th}} = 1$ PBH merger with $\Delta z_{\vee,\mathrm{th}} = 30$, but the impact is much less pronounced than for the other science metrics as the LIGO-India detector is not sensitive enough to detect most of the very-high-redshift BBH signals. These results are expected since the lower redshift error bound $\Delta z_{\vee,\mathrm{th}} = z(D_{\mathrm{L}} - \Delta D_{\mathrm{L}})$ directly depends on the luminosity distance error ΔD_{L} which, as a localization metric, is very sensitive to the number of detectors in the network.

These results on the discernability of PBH binary mergers appear more optimistic than what has been found in [72]. This seeming discrepancy is a result of the assumptions made in the underlying PBH mass distribution, favoring heavy binary systems with louder signals and improved distance/redshift estimation.

3.4. Sensitivity to power-law stochastic backgrounds

The following observing scenarios relevant to stochastic searches are investigated:

- the ET-2L detectors are online before the CE detector (top left panel of figure 5);
- the ET-△ detector is online before the CE detector (top right panel of figure 5);
- A single ET-L detector and the I+ detector are online, followed by a second ET-L (bottom left panel of figure 5);
- The CE detector and the I+ detector are online, followed by the ET-2L detectors (bottom right panel of figure 5).

In all these cases, it is assumed that the second detector comes online with a delay of $3N$ months and the PI curve is re-computed for each N, with N spanning $0 - 12$. This implies each curve should be interpreted as a total observing time of 3 years, where only a sub-set of detectors were online for the first $3N$ months, while the full network is online for $3(12 - N)$ months.

The first two cases considered highlight the impact of observing a stochastic signal with two or more XG detectors. Since stochastic searches require at least two detectors with (approximately) uncorrelated noise to construct the cross-correlation statistic [38, 75, 76], one cannot study the impact of having a single detector as this would require a significantly different statistic, incompatible with the definition of PI curves used here (equation (4)); therefore, the case of a single CE detector observing before being joined by the ET detectors cannot be studied. Here, ET-2L is considered to consist of two detectors with uncorrelated noise, while ET-△ to be comprised of two co-located independent detectors with uncorrelated noise. The latter is an optimistic approximation inspired by [77] and commonly used in the literature [23].

In the case of ET-2L, the addition of CE to the network moderately impacts the sensitivity to a stochastic signal; if CE comes online within an observing time of 3 years, the final sensitivity can be impacted up to a factor of ∼5, as shown in the top left panel of figure 5. Conversely, in the case of ET-△ considered here, CE would have a weak impact on the observation, as seen in the top right panel of figure 5. This difference is due to the fact that the suppression of the signal due to the overlap reduction function γ_{IJ} (cf equation (4)) is proportional to the distance between detectors, implying that co-located yet uncorrelated detectors provide the ideal observing strategy for backgrounds.

The second set of cases considered compare the performance of a hybrid network where an XG detector is initially observing coherently with a current-generation detector, and subsequently a second XG detector joins the observing campaign. As in the studies presented above, LIGO India is considered

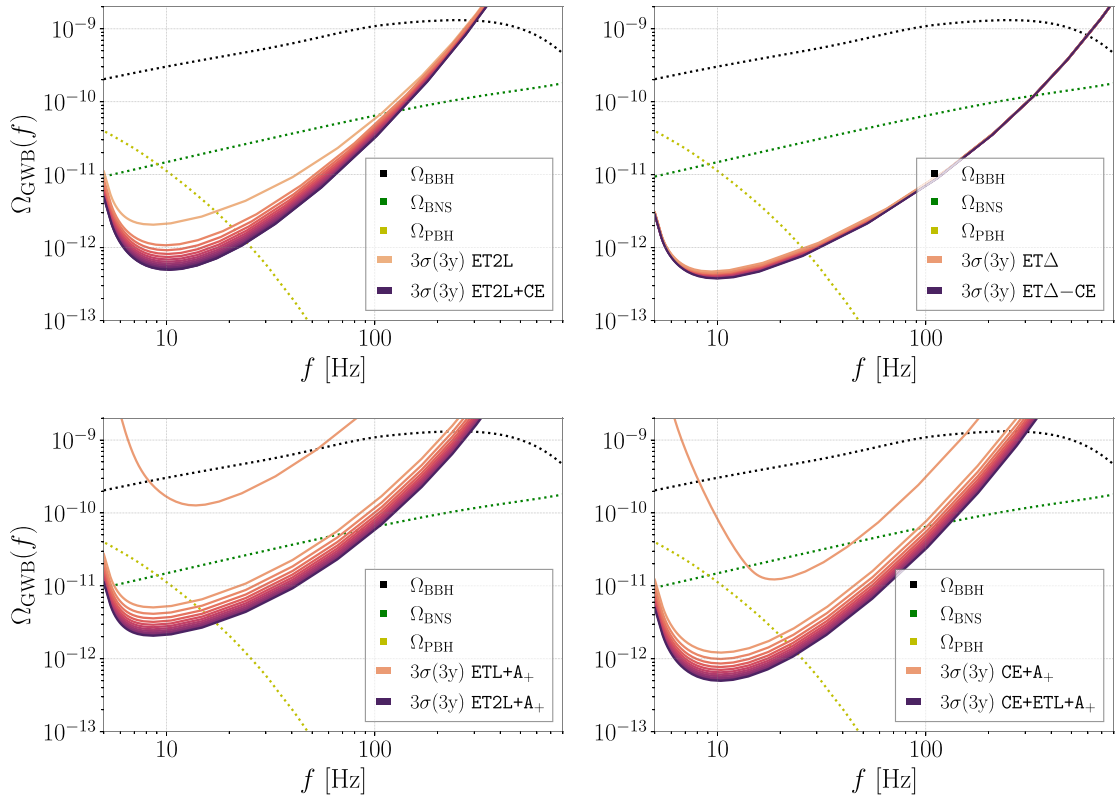

Figure 5. Power-law integrated (PI) curves for different XG networks, always considering a first set of detectors are online followed by a second detector with a delay of $3N$ months: the ET-2L detectors, followed by the CE detector (top left); the ET-$\triangle$ detector, followed by the CE detector (top right); a single ET-L detector and the I+ detector, followed by a second ET-L (bottom left); the CE detector and the I+ detector, followed by the ET-2L detectors. In all cases, each curve represents a 3 year observation where the first set of detectors are online for the first $3N$ months, while the full network is online for $3(12-N)$ months. The dotted lines represent the GWB spectral density $\Omega^{\rm CBC}_{\rm GWB}(f)$ calculated for each CBC population considered here.

for this purpose. After verifying that, in the configurations considered, there is no significant difference between assuming I+ versus I# sensitivity, only the results for I+ are presented.

As shown in the bottom panels of figure 5, adding a second XG detector to the network has a very significant impact to the network stochastic sensitivity. In the first case, adding a second ET-L to the ET-L −I+ network increases the sensitivity by a factor of ~ 50 almost instantly, as seen in the left panel. In the second case considered, adding ET-2L to the CE+I+ network increases the sensitivity by an order of magnitude. Similarly to directional studies discussed above, a network with at least two XG detectors is a substantially different network to one with a single XG, even when operating jointly with current-generation detectors.

For reference, figure 5 includes the total GWB signals from the three populations considered in this work, $\Omega^{\rm BBH}_{\rm GWB}(f)$, $\Omega^{\rm BNS}_{\rm GWB}(f)$, $\Omega^{\rm PBH}_{\rm GWB}(f)$, calculated as in equation (7). Note that a large portion of the signals that make up these background spectra will be individually resolvable, hence in a realistic detection scenario, the relevant stochastic portion of these signals may be the result of signal subtraction or simultaneously estimated with resolved components, as discussed in [56, 78–85]. Nevertheless, this study points out that all three of these spectra appear significantly detectable, in the case where at least two XG detectors are cross-correlated, and population characterisation studies employing the stochastic signal only may be performed, as suggested in [86]. On the other hand, as seen in Figure 5, a single XG detector correlated with a 2G detector is likely to detect the louder BBH background but would not be able to measure the neutron star and primordial signals.

4. Conclusions

In summary, purely SNR-dependent quantities are not affected, or only very marginally, by the timings of XG GW detector facilities within a network. A single XG facility will quickly deliver most of the science output that revolves around those targets. This includes studies aimed at constraining the observed populations of compact binaries [33], as well as testing GR via e.g. black-hole spectroscopy [12, 87, 88].

On the other hand, long-term delays in or asynchronous operation of the component facilities should be expected to significantly impact observation campaigns for any quantities in GW astronomy that strongly correlate or depend on the localization metrics, sky area and luminosity distance error. Crucially, this includes all multi-messenger applications, although modern, innovative optical telescopes such as the Vera C. Rubin Observatory could help mitigate the impact of delays to some degree, see [89]. In these cases, the observation times $T_{\rm obs}$ for networks containing both ET and CE configurations are orders of magnitude shorter than for networks with only one XG facility and any delay in the observation campaign of one of the component facilities is equivalent to a network-wide interruption for these metrics. Moreover, some configurations, notably those consisting of a single XG detector alone, would not be able to meet some of the related science requirements.

The addition of LIGO-India, in either the `I+` or `I#` configuration, while distinctly less sensitive than the XG facilities, presents a significant opportunity for softening the impact of such delays in the XG detector facilities, particularly for the strongly affected localization metrics. As expected and well understood [26], the addition of LIGO-India in either configuration would have negligible impact on the SNR metrics which will be dominated by the XG facilities. These conclusions would likely hold for any other of the existing detectors, if kept online while the XG networks commence observations and if operated at the investigated sensitivities.

Only primordial stellar-mass black holes are expected to merge at redshifts $z \gtrsim 30$ and thus a confident detection at redshifts beyond that threshold would serve as evidence for PBHs. The results of this study show that this metric requires at least two XG detectors in the network, `ET-2L` `ET-`$\triangle$ $+$ `CE`, or `ET-2L` $+$ `CE`, to confidently observe and discern that BBH merger events originate from redshifts $z \geqslant 30$. The addition of LIGO-India in A# configuration would only enable the `ET-`$\triangle$ configuration to observe a few PBH merger events at such high redshifts. However, even the detection of a single PBH binary would bring about a paradigm shift in the fields of dark matter and early-Universe cosmology.

Finally, the impact of different hybrid networks on the detectability of a stochastic signal was assessed. In particular it was shown that having at least two XG facilities online at the same time considerably accelerates detection and characterisation of GW backgrounds, including signals from different compact binary populations.

This study has several limitations. First and foremost, the Fisher information formalism is not as robust as full Bayesian parameter estimation and therefore single-event statistics can be misleading. This has been mitigated by focusing on a target of $N_{\rm th} = 10$ signals fulfilling the thresholds per metric and further through bootstrapping the simulated populations. Further, this study is limited to SNR and localization dependent metrics, discarding intrinsic GW parameters such as black hole or neutron star masses and spins, spin precession, orbital eccentricity, or neutron star tidal deformability, but also extrinsic phenomenologies concerning cosmology and astrophysical populations [33]. Additionally, the investigation of facility-wide timing delays does not take into account that the multi-detector ET facilities `ET-`$\triangle$ and `ET-2L` could experience such a delay in a single component detector only; it is implicitly assumed that the ET commissioning bodies will ensure simultaneous operation of all component detectors. Finally, it is assumed that all facilities under consideration commence observations at their design or target sensitivities. While this is common practice for forecasting studies, it is more relevant in the presented context of timing delays between facilities since the application of very optimistic sensitivity curves from the onset of observations could exacerbate the impact of such delays, as can be seen in [90].

Taken together, the results of this paper show that a single XG facility can indeed deliver a portion of the targeted science. However, some of the crucial elements of the XG science case require both ET and CE. Cooperation is the real key to success for GW astronomy in the coming decades.

Acknowledgments

We thank Rodrigo Tenorio and Riccardo Buscicchio for discussions. S B, P C, A R, C P, and D G are supported by ERC Starting Grant No. 945155–GWmining, Cariplo Foundation Grant No. 2021-0555, MUR PRIN Grant No. 2022-Z9X4XS, Italian-French University (UIF/UFI) Grant No. 2025-C3-386, MUR Grant 'Progetto Dipartimenti di Eccellenza 2023-2027' (BiCoQ), and the ICSC National Research Centre funded by NextGenerationEU. A R and D G are supported by MSCA Fellowships

No. 101064542–StochRewind. D G is supported by MSCA Fellowship No. 101149270–ProtoBH and MUR Young Researchers Grant No. SOE2024-0000125. M.M. is supported by the French government under the France 2030 investment plan, as part of the Initiative d'Excellence d'Aix-Marseille Université – A*MIDEX AMX-22-CEI-02. Computational work was performed at CINECA with allocations through INFN and the University of Milano-Bicocca, and at NVIDIA with allocations through the Academic Grant program.

Data availability statement

The data cannot be made publicly available upon publication because the cost of preparing, depositing and hosting the data would be prohibitive within the terms of this research project. The data that support the findings of this study are available upon reasonable request from the authors.

Appendix A. Detector specifications

The exact detector specifications can found in the dictionary at https://gitlab.com/sborhanian/gwbench/-/blob/master/gwbench/utils.py?ref_type = heads#L81 with the following keys used for the various studied detector facilities:

- 'ETS1', 'ETS2', 'ETS3' for the `ET-△`,
- 'ETN' and 'ETS' for `ET-2L`,
- 'CEA' for `CE`,
- 'I' for `I+` and `I#`.

Appendix B. Accompanying tables to the figures

Tables B1, B2, and B3 collect the expected observation times $T_{\rm obs}$ represented by markers across Figures 2 and 3 for all studied detector and network configurations, as well as the targeted thresholds for the SNR, sky area, luminosity distance error, comoving error volume, post-merger SNR, early-warning SNR, and early-warning sky area metrics.

Table B1. Companion table for estimated observation times $T_{\rm obs}$ for BBHs collecting the same information as shown across the top row of figure 2 and the left panel of figure 3. Each entry in the table corresponds to a marker in the figures for detector and network configurations ET-△, ET-△ + I+, ET-△ + I#, ET-△ + CE, ET-2L, ET-2L + I+, ET-2L + I#, ET-2L + CE, CE, CE + I+, and CE + I#.

	$\rho_{\rm th}$			$\Omega_{\rm th}$ [deg^2]			$(\Delta D_{\rm L}/D_{\rm L})_{\rm th}$		
$T_{\rm obs}^{\rm BBH}$ [yr]	100	300	1000	10	1	0.1	0.1	0.01	0.005
ET-△ + I#	0.0099	0.33	>5	0.0057	0.17	>5	0.00 087	0.55	5
ET-△ + I+	0.01	0.34	>5	0.013	0.46	>5	0.0013	1	>5
ET-△	0.01	0.35	>5	0.65	>5	>5	0.054	>5	>5
ET-△ + CE ($f_{\rm gap} = 0.75$)			2.8		0.76	0.98		0.81	1.4
ET-△ + CE ($f_{\rm gap} = 0.5$)			2.6	0.5	0.51	0.72		0.57	1.2
ET-△ + CE ($f_{\rm gap} = 0.25$)		0.26	2.4	0.25	0.26	0.49		0.31	0.9
ET-△ + CE ($f_{\rm gap} = 0.083$)		0.12	2.3	0.084	0.091	0.3		0.14	0.77
ET-△ + CE	0.002	0.048	2.1	0.00 044	0.0077	0.21	0.0003	0.069	0.7
ET-2L + I#	0.005	0.14	>5	0.0018	0.04	1.3	0.00 044	0.18	1.6
ET-2L + I+	0.0051	0.14	>5	0.004	0.096	2.4	0.00 054	0.23	1.9
ET-2L	0.0051	0.14	>5	0.034	1.2	>5	0.0018	1.3	>5
ET-2L + CE ($f_{\rm gap} = 0.75$)			2.1		0.75	0.88		0.77	1.1
ET-2L + CE ($f_{\rm gap} = 0.5$)			1.9		0.5	0.63		0.52	0.87
ET-2L + CE ($f_{\rm gap} = 0.25$)			1.7		0.25	0.39		0.28	0.64
ET-2L + CE ($f_{\rm gap} = 0.083$)		0.1	1.6		0.088	0.21		0.12	0.52
ET-2L + CE	0.0016	0.038	1.5	0.00 033	0.005	0.13	0.00 023	0.043	0.44
CE + I#	0.0029	0.074	2.9	0.015	0.39	>5	0.0043	2.4	>5
CE + I+	0.0029	0.075	2.9	0.073	2	>5	0.0088	>5	>5
CE	0.0029	0.076	2.9	>5	>5	>5	>5	>5	>5
CE + ET-△ ($f_{\rm gap} = 0.75$)			2.4	0.75	0.76	0.98	0.75	0.81	1.4
CE + ET-△ ($f_{\rm gap} = 0.5$)			2.3	0.5	0.51	0.72	0.5	0.57	1.2
CE + ET-△ ($f_{\rm gap} = 0.25$)			2.2	0.25	0.26	0.49	0.25	0.31	0.9
CE + ET-△ ($f_{\rm gap} = 0.083$)			2.2	0.084	0.091	0.3	0.084	0.14	0.77
CE + ET-△	0.002	0.048	2.1	0.00 044	0.0077	0.21	0.0003	0.069	0.7
CE + ET-2L ($f_{\rm gap} = 0.75$)			1.9	0.75	0.75	0.88	0.75	0.79	1.2
CE + ET-2L ($f_{\rm gap} = 0.5$)			1.8	0.5	0.5	0.63	0.5	0.54	0.9
CE + ET-2L ($f_{\rm gap} = 0.25$)			1.6	0.25	0.25	0.39	0.25	0.29	0.67
CE + ET-2L ($f_{\rm gap} = 0.083$)			1.5	0.084	0.088	0.21	0.084	0.12	0.52
CE + ET-2L	0.0016	0.038	1.5	0.00 033	0.005	0.13	0.00 023	0.043	0.44

	$\rho_{\rm pm,th}$						$V_{\rm th}$ [Mpc^3]		
	20	60	200				100	10	1
ET-△ + I#	0.0085	0.39	>5				>5	>5	>5
ET-△ + I+	0.0087	0.41	>5				>5	>5	>5
ET-△	0.0088	0.41	>5				>5	>5	>5
ET-△ + CE ($f_{\rm gap} = 0.75$)			>5				2.6	>5	>5
ET-△ + CE ($f_{\rm gap} = 0.5$)			>5				2.4	>5	>5
ET-△ + CE ($f_{\rm gap} = 0.25$)		0.3	>5				2.1	>5	>5
ET-△ + CE ($f_{\rm gap} = 0.083$)		0.17	>5				1.9	>5	>5
ET-△ + CE	0.0029	0.096	>5				1.9	>5	>5
ET-2L + I#	0.0043	0.15	>5				3	>5	>5
ET-2L + I+	0.0045	0.15	>5				5	>5	>5

(Continued.)

Table B1. (Continued.)

	$\rho_{\rm th}$			$\Omega_{\rm th}$ [deg^2]			$(\Delta D_{\rm L}/D_{\rm L})_{\rm th}$		
$T_{\rm obs}^{\rm BBH}$ [yr]	100	300	1000	10	1	0.1	0.1	0.01	0.005
ET-2L	0.0045	0.15	>5				>5	>5	>5
ET-2L + CE ($f_{\rm gap} = 0.75$)			>5				2	>5	>5
ET-2L + CE ($f_{\rm gap} = 0.5$)			>5				1.8	4.7	>5
ET-2L + CE ($f_{\rm gap} = 0.25$)			>5				1.5	4.2	>5
ET-2L + CE ($f_{\rm gap} = 0.083$)		0.11	>5				1.4	4.2	>5
ET-2L + CE	0.0022	0.061	>5				1.4	4.3	>5
CE + I#	0.0053	0.2	>5				>5	>5	>5
CE + I+	0.0057	0.2	>5				>5	>5	>5
CE	0.0057	0.2	>5				>5	>5	>5
CE + ET-△ ($f_{\rm gap} = 0.75$)			>5				2.6	>5	>5
CE + ET-△ ($f_{\rm gap} = 0.5$)			>5				2.4	>5	>5
CE + ET-△ ($f_{\rm gap} = 0.25$)			>5				2.1	>5	>5
CE + ET-△ ($f_{\rm gap} = 0.083$)		0.14	>5				1.9	>5	>5
CE + ET-△	0.0029	0.096	>5				1.9	>5	>5
CE + ET-2L ($f_{\rm gap} = 0.75$)			>5				2	>5	>5
CE + ET-2L ($f_{\rm gap} = 0.5$)			>5				1.8	4.7	>5
CE + ET-2L ($f_{\rm gap} = 0.25$)			>5				1.5	4.2	>5
CE + ET-2L ($f_{\rm gap} = 0.083$)		0.12	>5				1.4	4.2	>5
CE + ET-2L	0.0022	0.061	>5				1.4	4.3	>5

Table B2. Companion table for estimated observation times $T_{\rm obs}$ for BNSs collecting the same information as shown across the bottom row of figure 2 and the right panel of figure 3. Each entry in the table corresponds to a marker in the figures for detector and network configurations ET-△, ET-△ + I+, ET-△ + I#, ET-△ + CE, ET-2L, ET-2L + I+, ET-2L + I#, ET-2L + CE, CE, CE + I+, and CE + I#.

	$\rho_{\rm th}$			$\Omega_{\rm th}$ [deg^2]			$(\Delta D_{\rm L}/D_{\rm L})_{\rm th}$		
$T_{\rm obs}^{\rm BNS}$ [yr]	50	200	400	10	1	0.1	0.2	0.1	0.01
ET-△ + I#	0.14	>5	>5	0.32	>5	>5	0.0033	0.048	>5
ET-△ + I+	0.14	>5	>5	0.76	>5	>5	0.0038	0.068	>5
ET-△	0.15	>5	>5	2.5	>5	>5	0.013	0.4	>5
ET-△ + CE ($f_{\rm gap} = 0.75$)		2.2	>5	0.76	1.2	>5			>5
ET-△ + CE ($f_{\rm gap} = 0.5$)		2	>5	0.51	0.99	>5			>5
ET-△ + CE ($f_{\rm gap} = 0.25$)		1.8	>5	0.27	0.75	>5		0.25	>5
ET-△ + CE ($f_{\rm gap} = 0.083$)	0.092	1.6	>5	0.1	0.58	>5		0.091	>5
ET-△ + CE	0.021	1.6	>5	0.017	0.49	>5	0.00 096	0.012	>5
ET-2L + I#	0.06	4.3	>5	0.073	2.6	>5	0.0015	0.017	>5
ET-2L + I+	0.061	4.3	>5	0.17	>5	>5	0.0017	0.023	>5
ET-2L	0.062	4.3	>5	1.1	>5	>5	0.0033	0.052	>5
ET-2L + CE ($f_{\rm gap} = 0.75$)		1.8	>5	0.75	1.1	>5			>5
ET-2L + CE ($f_{\rm gap} = 0.5$)		1.6	>5	0.51	0.84	>5			>5
ET-2L + CE ($f_{\rm gap} = 0.25$)		1.3	>5	0.26	0.56	>5			>5
ET-2L + CE ($f_{\rm gap} = 0.083$)		1.2	>5	0.093	0.4	>5			4.9
ET-2L + CE	0.016	1.2	>5	0.01	0.33	>5	0.00 065	0.0065	5
CE + I#	0.033	2.3	>5	1.5	>5	>5	0.057	2.7	>5
CE + I+	0.034	2.3	>5	5	>5	>5	0.11	>5	>5
CE	0.034	2.3	>5	>5	>5	>5	>5	>5	>5

(Continued.)

Table B2. (Continued.)

CE + ET-△ ($f_{\rm gap} = 0.75$)		1.8	>5	0.77	1.2	>5	0.75	0.76	>5
CE + ET-△ ($f_{\rm gap} = 0.5$)		1.7	>5	0.52	0.99	>5	0.5	0.51	>5
CE + ET-△ ($f_{\rm gap} = 0.25$)		1.6	>5	0.27	0.75	>5	0.25	0.26	>5
CE + ET-△ ($f_{\rm gap} = 0.083$)		1.6	>5	0.1	0.58	>5	0.084	0.094	>5
CE + ET-△	0.021	1.6	>5	0.017	0.49	>5	0.00 096	0.012	>5
CE + ET-2L ($f_{\rm gap} = 0.75$)		1.5	>5	0.76	1.1	>5	0.75	0.76	>5
CE + ET-2L ($f_{\rm gap} = 0.5$)		1.4	>5	0.51	0.84	>5	0.5	0.51	>5
CE + ET-2L ($f_{\rm gap} = 0.25$)		1.3	>5	0.26	0.56	>5	0.25	0.26	>5
CE + ET-2L ($f_{\rm gap} = 0.083$)		1.2	>5	0.094	0.4	>5	0.084	0.089	4.9
CE + ET-2L	0.016	1.2	>5	0.01	0.33	>5	0.00 065	0.0065	5

	$\rho_{\rm ew,th}$			$\Omega_{\rm ew,th}$ [deg^2]			$V_{\rm th}$ [Mpc^3]		
	20	80	160	10	1	0.1	1000	100	10
ET-△ + I#	0.037	2.4	>5	>5	>5	>5	>5	>5	>5
ET-△ + I+	0.037	2.4	>5	>5	>5	>5	>5	>5	>5
ET-△	0.037	2.4	>5	>5	>5	>5	>5	>5	>5
ET-△ + CE ($f_{\rm gap} = 0.75$)		1	3.2	1.8	>5	>5	4	>5	>5
ET-△ + CE ($f_{\rm gap} = 0.5$)		0.77	3.3	1.5	>5	>5	3.6	>5	>5
ET-△ + CE ($f_{\rm gap} = 0.25$)		0.54	2.8	1.3	>5	>5	3.3	>5	>5
ET-△ + CE ($f_{\rm gap} = 0.083$)		0.4	2.7	1.2	>5	>5	2.9	>5	>5
ET-△ + CE	0.0075	0.32	2.6	1.1	>5	>5	2.8	>5	>5
ET-2L + I#	0.019	1.2	>5	>5	>5	>5	>5	>5	>5
ET-2L + I+	0.019	1.2	>5	>5	>5	>5	>5	>5	>5
ET-2L	0.019	1.2	>5	>5	>5	>5	>5	>5	>5
ET-2L + CE ($f_{\rm gap} = 0.75$)		0.85	2.7	1.3	>5	>5	2.8	>5	>5
ET-2L + CE ($f_{\rm gap} = 0.5$)		0.65	2.5	1.1	>5	>5	2.5	>5	>5
ET-2L + CE ($f_{\rm gap} = 0.25$)		0.46	2.4	0.9	>5	>5	2.4	>5	>5
ET-2L + CE ($f_{\rm gap} = 0.083$)		0.33	2.2	0.77	>5	>5	2.2	>5	>5
ET-2L + CE	0.006	0.27	2.2	0.66	>5	>5	2.1	>5	>5
CE + I#	0.011	0.48	3.7	>5	>5	>5	>5	>5	>5
CE + I+	0.011	0.48	3.7	>5	>5	>5	>5	>5	>5
CE	0.011	0.48	3.7	>5	>5	>5	>5	>5	>5
CE + ET-△ ($f_{\rm gap} = 0.75$)			2.8	1.8	>5	>5	4	>5	>5
CE + ET-△ ($f_{\rm gap} = 0.5$)			2.8	1.6	>5	>5	3.6	>5	>5
CE + ET-△ ($f_{\rm gap} = 0.25$)		0.4	2.7	1.3	>5	>5	3.3	>5	>5
CE + ET-△ ($f_{\rm gap} = 0.083$)		0.36	2.6	1.2	>5	>5	2.9	>5	>5
CE + ET-△	0.0075	0.32	2.6	1.1	>5	>5	2.8	>5	>5
CE + ET-2L ($f_{\rm gap} = 0.75$)			2.4	1.4	>5	>5	2.8	>5	>5
CE + ET-2L ($f_{\rm gap} = 0.5$)			2.4	1.2	>5	>5	2.5	>5	>5
CE + ET-2L ($f_{\rm gap} = 0.25$)		0.37	2.4	0.94	>5	>5	2.4	>5	>5
CE + ET-2L ($f_{\rm gap} = 0.083$)		0.31	2.2	0.77	>5	>5	2.2	>5	>5
CE + ET-2L	0.006	0.27	2.2	0.66	>5	>5	2.1	>5	>5

Table B3. Companion table for estimated observation times $T_{\rm obs}$ for BNSs collecting the same information as shown across figures 2 and 3. Each entry in the table corresponds to a marker in the figures for detector and network configurations CE + ET-△, CE + ET-△ + I+, CE + ET-△ + I#, CE + ET-2L, CE + ET-2L + I+, and CE + ET-2L + I#.

	$\rho_{\rm th}$			$\Omega_{\rm th}$ [deg^2]			$(\Delta D_{\rm L}/D_{\rm L})_{\rm th}$		
$T_{\rm obs}^{\rm BBH}$ [yr]	100	300	1000	10	1	0.1	0.1	0.01	0.005
CE + ET-△	0.002	0.048	2.1	0.00 044	0.0077	0.21	0.0003	0.069	0.7
CE + ET-△ + I+	0.002	0.048	2.1	0.00 033	0.0049	0.14	0.00 028	0.062	0.66
CE + ET-△ + I#	0.002	0.047	2.1	0.00 028	0.0033	0.081	0.00 027	0.054	0.63
CE + ET-2L	0.0016	0.038	1.5	0.00 033	0.005	0.13	0.00 023	0.043	0.44
CE + ET-2L + I+	0.0016	0.038	1.5	0.00 028	0.0037	0.1	0.00 022	0.039	0.4
CE + ET-2L + I#	0.0016	0.038	1.5	0.00 023	0.0026	0.062	0.00 021	0.036	0.38

	$\rho_{\rm pm,th}$			$V_{\rm th}$ [Mpc^3]		
	20	60	200	100	10	1
CE + ET-△	0.0029	0.096	>5	1.9	>5	>5
CE + ET-△ + I+	0.0029	0.096	>5	1.5	4.3	>5
CE + ET-△ + I#	0.0028	0.093	>5	1.2	3.3	>5
CE + ET-2L	0.0022	0.061	>5	1.4	4.3	>5
CE + ET-2L + I+	0.0022	0.06	>5	1.2	3.7	>5
CE + ET-2L + I#	0.0021	0.057	>5	1	2.8	>5

	$\rho_{\rm th}$			$\Omega_{\rm th}$ [deg^2]			$(\Delta D_{\rm L}/D_{\rm L})_{\rm th}$		
$T_{\rm obs}^{\rm BNS}$ [yr]	50	200	400	10	1	0.1	0.2	0.1	0.01
CE + ET-△	0.021	1.6	>5	0.017	0.49	>5	0.00 096	0.012	>5
CE + ET-△ + I+	0.021	1.6	>5	0.0087	0.27	>5	0.00 086	0.0091	>5
CE + ET-△ + I#	0.021	1.4	>5	0.0048	0.14	5	0.00 081	0.008	>5
CE + ET-2L	0.016	1.2	>5	0.01	0.33	>5	0.00 065	0.0065	5
CE + ET-2L + I+	0.016	1.2	>5	0.0063	0.19	>5	0.00 062	0.0054	4.3
CE + ET-2L + I#	0.016	1.2	>5	0.004	0.12	3.7	0.00 058	0.0049	4.3

	$\rho_{\rm ew,th}$			$\Omega_{\rm ew,th}$ [deg^2]			$V_{\rm th}$ [Mpc^3]		
	20	80	160	10	1	0.1	1000	100	10
CE + ET-△	0.0075	0.32	2.6	1.1	>5	>5	2.8	>5	>5
CE + ET-△ + I+	0.0075	0.32	2.6	1	>5	>5	2.1	>5	>5
CE + ET-△ + I#	0.0075	0.32	2.6	1	>5	>5	1.7	>5	>5
CE + ET-2L	0.006	0.27	2.2	0.66	>5	>5	2.1	>5	>5
CE + ET-2L + I+	0.006	0.27	2.2	0.66	>5	>5	1.6	>5	>5
CE + ET-2L + I#	0.006	0.27	2.2	0.63	>5	>5	1.4	>5	>5

Appendix C. Full observation time maps

Figures C1, C2, and C3 present full maps of $N_{\rm th}$ against a range of threshold values for all the studied metrics for BBH, BNS, and PBH mergers: the SNR $\rho_{\rm th}$, sky area $\Omega_{\rm th}$, relative luminosity distance error $(\Delta D_{\rm L}/D_{\rm L})_{\rm th}$, comoving error volume $V_{\rm th}$, post-merger SNR $\rho_{\rm pm,th}$ for BBHs, early-warning SNR $\rho_{\rm ew,th}$ and early-warning sky area $\Omega_{\rm ew,th}$ for BNSs, and the lower redshift error bound $\Delta z_{\rm V,th}$ for PBHs. The maps are binned into eight human-experiment-scale time frames, with the nineth bin corresponding to observation times exceeding five years.

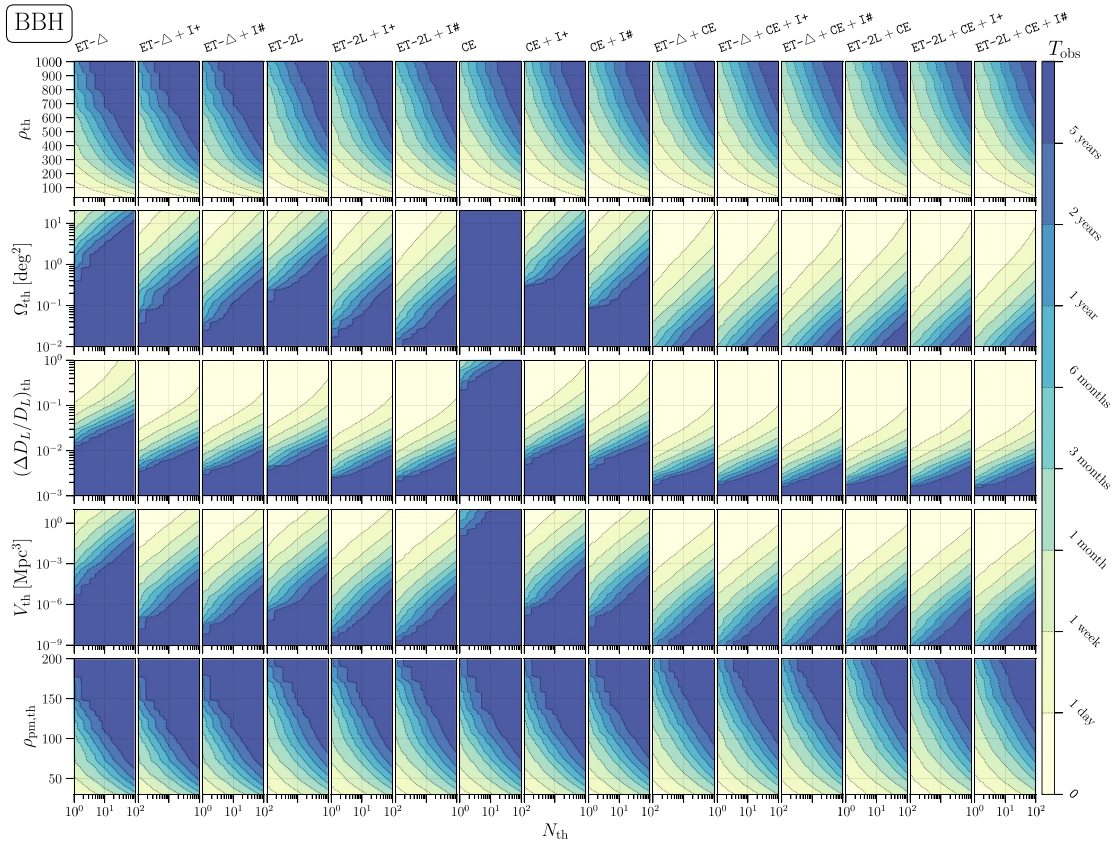

Figure C1. Maps of expected observation times $T_{\rm obs}$ to reach a target of at least $N_{\rm th}$ BBH signals satisfying a threshold for SNR $\rho_{\rm th}$, post-merger SNR $\rho_{\rm pm,th}$, sky area $\Omega_{\rm th}$, relative luminosity distance error $(\Delta D_{\rm L}/D_{\rm L})_{\rm th}$, or comoving error volume $V_{\rm th}$, observed with 15 different XG, ground-based GW detector networks. Quantities $N_{\rm th}$, $\rho_{\rm th}$, $\rho_{\rm pm,th}$ and $\Omega_{\rm th}$, $(\Delta D_{\rm L}/D_{\rm L})_{\rm th}$, $V_{\rm th}$ represent lower and upper thresholds, respectively. The observing time $T_{\rm obs}$ is calculated for a fiducial cosmic merger rate of $\mathcal{R} = 10^5\,{\rm yr}^{-1}$ and is binned into eight human-experiment-scale time frames, with the nineth bin corresponding to observation times exceeding five years. The merger events are Poisson-distributed and 100-fold bootstrapped from 10^6 simulated signals.

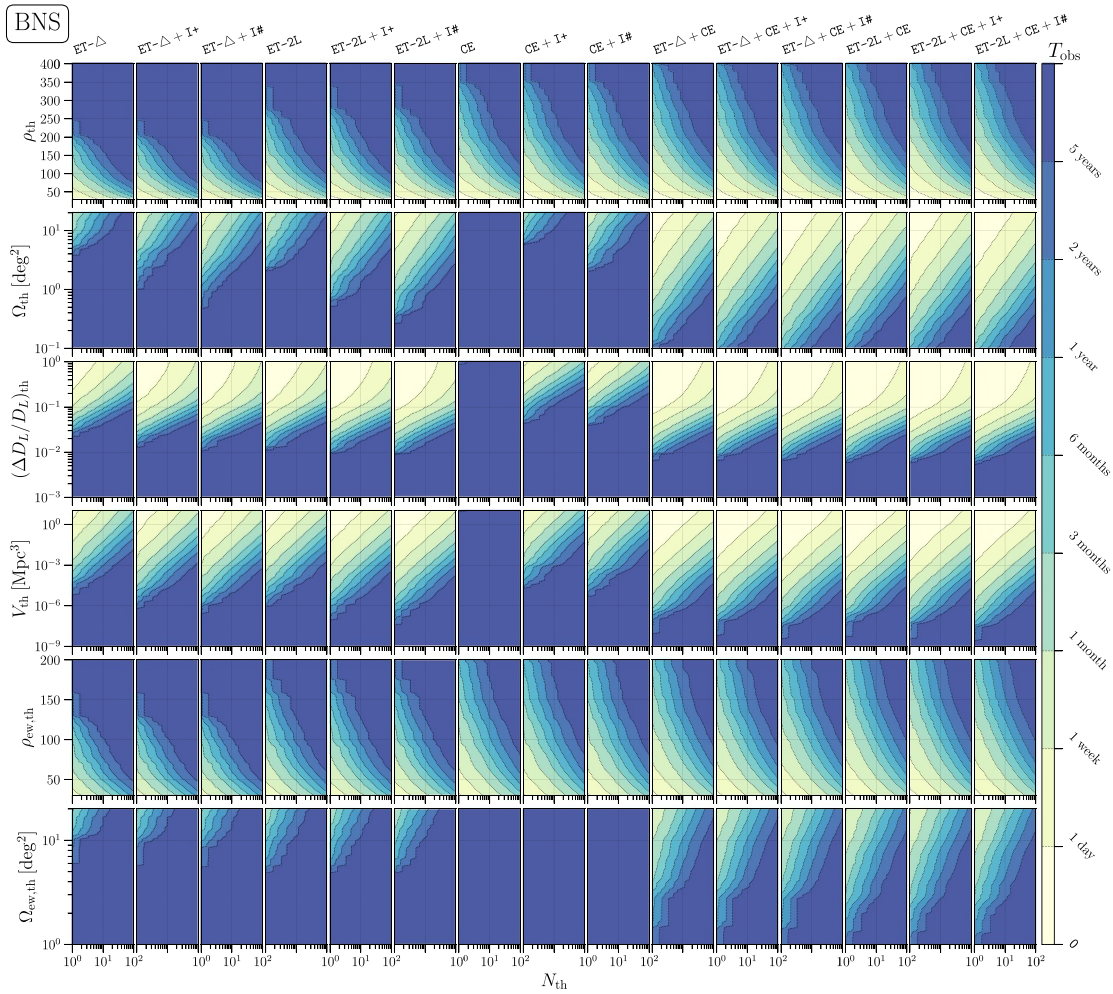

Figure C2. Maps of expected observation times $T_{\rm obs}$ to reach a target of at least $N_{\rm th}$ BBH signals satisfying a threshold for SNR $\rho_{\rm th}$, early-warning SNR $\rho_{\rm ew,th}$, sky area $\Omega_{\rm th}$, early-warning sky area $\Omega_{\rm ew,th}$, relative luminosity distance error $(\Delta D_{\rm L}/D_{\rm L})_{\rm th}$, or comoving error volume $V_{\rm th}$, observed with 15 different XG, ground-based GW detector networks. Quantities $N_{\rm th}$, $\rho_{\rm th}$, $\rho_{\rm ew,th}$ and $\Omega_{\rm th}$, $\Omega_{\rm ew,th}$, $(\Delta D_{\rm L}/D_{\rm L})_{\rm th}$, $V_{\rm th}$ represent lower and upper thresholds, respectively. The observing time $T_{\rm obs}$ is calculated for a fiducial cosmic merger rate of $\mathcal{R} = 10^5\,{\rm yr}^{-1}$ and is binned into eight human-experiment-scale time frames, with the nineth bin corresponding to observation times exceeding five years. The merger events are Poisson-distributed and 100-fold bootstrapped from 10^6 simulated signals.

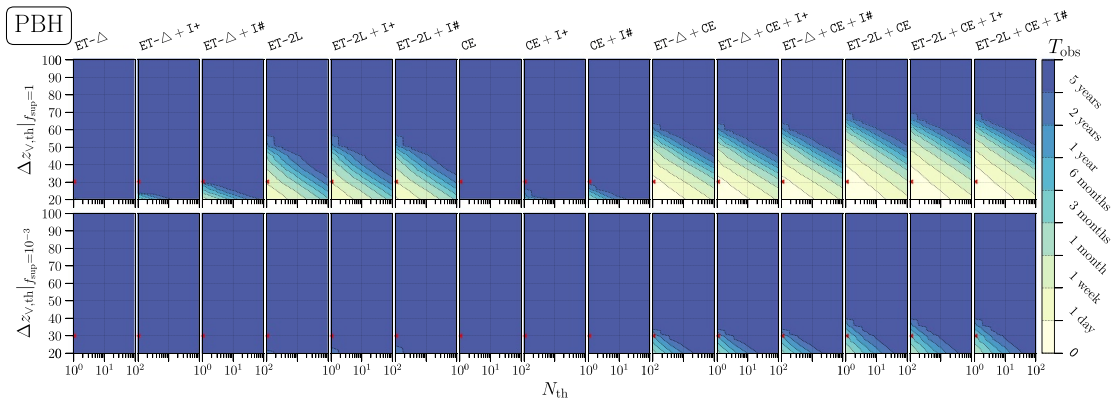

Figure C3. Maps of expected observation times $T_{\rm obs}$ to reach a target of at least $N_{\rm th}$ PBH signals satisfying varying thresholds for the lower redshift error bound $\Delta z_{\vee,\rm th}$ at two values for the PBH-formation suppression factor $f_{\rm sup} \in \{10^{-3}, 1\}$, observed with 15 different XG, ground-based GW detector networks. The observing time $T_{\rm obs}$ is calculated for a fiducial cosmic merger rate of $\mathcal{R} = 2 \times 10^5\,{\rm yr}^{-1}$ and is binned into eight human-experiment-scale time frames, with the nineth bin corresponding to observation times exceeding five years. The merger events are Poisson-distributed and 100-fold bootstrapped from 10^6 simulated signals. The red marker indicates the corresponding positions, $N_{\rm th} = 1$ and $\Delta z_{\vee,\rm th} = 30$ corresponding to figure 4.

ORCID iDs

Ssohrab Borhanian 0000-0003-0161-6109
Arianna Renzini 0000-0002-4589-3987
Philippa S Cole 0000-0001-6045-6358
Costantino Pacilio 0000-0002-8140-4992
Michele Mancarella 0000-0002-0675-508X
Davide Gerosa 0000-0002-0933-3579

References

[1] LIGO Scientific Collaboration and Advanced LIGO 2015 *Class. Quantum Grav.* **32** 074001
[2] VIRGO Collaboration 2015 Advanced Virgo: a second-generation interferometric gravitational wave detector *Class. Quantum Grav.* **32** 024001
[3] KAGRA Collaboration 2013 Interferometer design of the KAGRA gravitational wave detector *Phys. Rev. D* **88** 043007
[4] Unnikrishnan C S 2013 IndIGO and LIGO-India: scope and plans for gravitational wave research and precision metrology in India *Int. J. Mod. Phys. D* **22** 1341010
[5] LIGO Scientific, Virgo Collaboration 2019 GWTC-1: a gravitational-wave transient catalog of compact binary mergers observed by LIGO and Virgo during the first and second observing runs *Phys. Rev. X* **9** 031040
[6] LIGO Scientific, Virgo Collaboration 2021 GWTC-2: compact binary coalescences observed by LIGO and Virgo during the first half of the third observing run *Phys. Rev. X* **11** 021053
[7] LIGO Scientific, Virgo, KAGRA Collaboration 2023 GWTC-3: compact binary coalescences observed by LIGO and Virgo during the second part of the third observing run *Phys. Rev. X* **13** 041039
[8] LIGO Scientific, VIRGO, KAGRA Collaboration, GWTC-4.0: updating the gravitational-wave transient catalog with observations from the first part of the fourth LIGO-Virgo-KAGRA observing run (arXiv:2508.18082)
[9] LIGO Scientific, Virgo, KAGRA Collaboration 2016 Prospects for observing and localizing gravitational-wave transients with advanced LIGO, advanced Virgo and KAGRA *Living Rev. Relativ.* **19** 3
[10] Fritschel P *et al* 2022 Report from the LSC Post-O5 study group *Technical Report* LIGO-T2200287 (available at: https://dcc.ligo.org/LIGO-T2200287/public)
[11] Punturo M *et al* 2010 The Einstein telescope: a third-generation gravitational wave observatory *Class. Quantum Grav.* **27** 194002
[12] Abac A *et al* The science of the Einstein telescope *Technical Report* ET-0036C-25 2025 (arXiv:2503.12263)
[13] Reitze D *et al* 2019 Cosmic explorer: the U.S. contribution to gravitational-wave astronomy beyond LIGO Bull. Am. Astron. Soc. 51 035 (arXiv:1907.04833)
[14] Vitale S and Evans M 2017 Parameter estimation for binary black holes with networks of third generation gravitational-wave detectors *Phys. Rev. D* **95** 064052
[15] Singh N, Bulik T, Belczynski K and Askar A 2022 Exploring compact binary populations with the Einstein telescope *Astron. Astrophys.* **667** A2
[16] Borhanian S and Sathyaprakash B S 2024 Listening to the Universe with next generation ground-based gravitational-wave detectors *Phys. Rev. D* **110** 083040
[17] Iacovelli F, Mancarella M, Foffa S and Maggiore M 2022 Forecasting the detection capabilities of third-generation gravitational-wave detectors using GWFAST *Astrophys. J.* **941** 208
[18] Ronchini S *et al* 2022 Perspectives for multimessenger astronomy with the next generation of gravitational-wave detectors and high-energy satellites *Astron. Astrophys.* **665** A97
[19] Banerjee B *et al* 2023 Pre-merger alert to detect prompt emission in very-high-energy gamma-rays from binary neutron star mergers: Einstein telescope and Cherenkov telescope array synergy *Astron. Astrophys.* **678** A126
[20] Yi S-X, Stoppa F, Nelemans G and Cator E 2022 The gravitational wave Universe toolbox - II. constraining the binary black hole population with second and third generation detectors *Astron. Astrophys.* **663** A156
[21] Gupta I, Borhanian S, Dhani A, Chattopadhyay D, Kashyap R, Villar V A and Sathyaprakash B, 2023 Neutron star-black hole mergers in next generation gravitational-wave observatories *Phys. Rev. D* **107** 124007
[22] Santoliquido F, Dupletsa U, Tissino J, Branchesi M, Iacovelli F and Iorio G 2024 Classifying binary black holes from population III stars with the Einstein telescope: a machine-learning approach *Astron. Astrophys.* **690** A362
[23] Branchesi M *et al* 2023 Science with the Einstein telescope: a comparison of different designs *J. Cosmol. Astropart. Phys.* **07** 068
[24] Evans M *et al* 2021 A horizon study for cosmic explorer: science, observatories, and community *Technical Report* CE-P2100003 (available at: https://dcc.cosmicexplorer.org/CE-P2100003/public) (arXiv:2109.09882)
[25] Evans M *et al* Cosmic explorer: a submission to the NSF MPSAC ngGW subcommittee (arXiv:2306.13745)
[26] Vitale S and Whittle C 2018 Characterization of binary black holes by heterogeneous gravitational-wave networks *Phys. Rev. D* **98** 024029
[27] Pandey S, Gupta I, Chandra K and Sathyaprakash B S 2025 The critical role of LIGO-India in the era of next-generation observatories *Astrophys. J. Lett.* **985** L17
[28] Planck Collaboration 2020 Planck 2018 results. VI. cosmological parameters *Astron. Astrophys.* **641** A6
[29] Borhanian S 2021 GWBENCH: a novel Fisher information package for gravitational-wave benchmarking *Class. Quantum Grav.* **38** 175014
[30] Cutler C and Flanagan E E 1994 Gravitational waves from merging compact binaries: how accurately can one extract the binary's parameters from the inspiral wave form? *Phys. Rev. D* **49** 2658
[31] Poisson E and Will C M 1995 Gravitational waves from inspiraling compact binaries: parameter estimation using second post-Newtonian wave forms *Phys. Rev. D* **52** 848
[32] Balasubramanian R, Sathyaprakash B S and Dhurandhar S V 1996 Gravitational waves from coalescing binaries: detection strategies and Monte Carlo estimation of parameters *Phys. Rev. D* **53** 3033
[33] De Renzis V, Iacovelli F, Gerosa D, Mancarella M and Pacilio C 2025 Forecasting the population properties of merging black holes *Phys. Rev. D* **111** 044048

[34] Vallisneri M 2008 Use and abuse of the Fisher information matrix in the assessment of gravitational-wave parameter-estimation prospects *Phys. Rev. D* **77** 042001
[35] LIGO Scientific, VIRGO, KAGRA Collaboration GWTC-4.0: population properties of merging compact binaries (arXiv:2508.18083)
[36] Ivezić Ž, Connolly A J, VanderPlas J T and Gray A 2020 *Statistics, Data Mining and Machine Learning in Astronomy. A Practical Python Guide for the Analysis of Survey Data* (De Gruyter) https://doi.org/10.1515/9780691197050
[37] Thrane E and Romano J D 2013 Sensitivity curves for searches for gravitational-wave backgrounds *Phys. Rev. D* **88** 124032
[38] Romano J D and Cornish N J 2017 Detection methods for stochastic gravitational-wave backgrounds: a unified treatment *Rev. Relativ.* **20** 2
[39] García-Quirós C *et al* 2020 Multimode frequency-domain model for the gravitational wave signal from nonprecessing black-hole binaries *Phys. Rev. D* **102** 064002
[40] García-Quirós C, Husa S, Mateu-Lucena M and Borchers A 2021 Accelerating the evaluation of inspiral-merger-ringdown waveforms with adapted grids *Class. Quantum Grav.* **38** 015006
[41] Mihaylov D P, Ossokine S, Buonanno A and Ghosh A 2021 Fast post-adiabatic waveforms in the time domain: applications to compact binary coalescences in LIGO and Virgo *Phys. Rev. D* **104** 124087
[42] Ng K K Y, Vitale S, Farr W M and Rodriguez C L 2021 Probing multiple populations of compact binaries with third-generation gravitational-wave detectors *Astrophys. J. Lett.* **913** L5
[43] Madau P and Dickinson M 2014 Cosmic star formation history *Annu. Rev. Astron. Astrophys.* **52** 415
[44] LIGO Scientific and Virgo Collaboration 2021 Population properties of compact objects from the second LIGO-Virgo gravitational-wave transient catalog *Astrophys. J. Lett.* **913** L7
[45] Douchin F and Haensel P 2001 A unified equation of state of dense matter and neutron star structure *Astron. Astrophys.* **380** 151
[46] Ashton G *et al* 2019 BILBY: a user-friendly Bayesian inference library for gravitational-wave astronomy *Astrophys. J.* **241** 27
[47] Green A M 2024 Primordial black holes as a dark matter candidate - a brief overview *Nucl. Phys. B* **1003** 116494
[48] Escrivà A, Kuhnel F and Tada Y 2022 Primordial black holes *Black Holes in the Era of Gravitational-Wave Astronomy* (Elsevier) p 11
[49] Suyama T and Yoo C-M 2025 Overall picture: a beginner's guide to primordial black hole formation *Primordial Black Holes* (Springer) https://doi.org/10.1007/978-981-97-8887-3_2
[50] Andrés-Carcasona M *et al* 2024 Constraints on primordial black holes from LIGO-Virgo-KAGRA O3 events *Phys. Rev. D* **110** 023040
[51] Crescimbeni F *et al* 2025 The irrelevance of primordial black hole clustering in the LVK mass range *J. Cosmol. Astropart. Phys.* **05** 001
[52] Carr B, Clesse S, Garcia-Bellido J, Hawkins M and Kuhnel F 2024 Observational evidence for primordial black holes: a positivist perspective *Phys. Rep.* **1054** 1
[53] Cole P S and Byrnes C T 2018 Extreme scenarios: the tightest possible constraints on the power spectrum due to primordial black holes *J. Cosmol. Astropart. Phys.* **02** 019
[54] Chen Z-C and Hall A 2025 Confronting Primordial Black Holes with LIGO-Virgo-KAGRA and the Einstein Telescope *Primordial Black Holes* (Springer) https://doi.org/10.1007/978-981-97-8887-3_25
[55] Iacovelli F and Maggiore M 2025 Gravitational-wave observations and primordial black holes *Primordial Black Holes* (Springer) https://doi.org/10.1007/978-981-97-8887-3_15
[56] Martinovic K, Meyers P M, Sakellariadou M and Christensen N 2021 Simultaneous estimation of astrophysical and cosmological stochastic gravitational-wave backgrounds with terrestrial detectors *Phys. Rev. D* **103** 043023
[57] Raidal M, Spethmann C, Vaskonen V and Veermäe H 2019 Formation and evolution of primordial black hole binaries in the early Universe *J. Cosmol. Astropart. Phys.* **02** 018
[58] Raidal M, Vaskonen V and Veermäe H 2017 Gravitational waves from primordial black hole mergers *J. Cosmol. Astropart. Phys.* **09** 037
[59] Mukherjee S and Silk J 2021 Can we distinguish astrophysical from primordial black holes via the stochastic gravitational wave background? *Mon. Not. R. Astron. Soc.* **506** 3977
[60] Mukherjee S, Meinema M S P and Silk J 2022 Prospects of discovering subsolar primordial black holes using the stochastic gravitational wave background from third-generation detectors *Mon. Not. R. Astron. Soc.* **510** 6218
[61] Regimbau T 2011 The astrophysical gravitational wave stochastic background *Res. Astron. Astrophys.* **11** 369
[62] Callister T, Fishbach M, Holz D and Farr W 2020 Shouts and murmurs: combining individual gravitational-wave sources with the stochastic background to measure the history of binary black hole mergers *Astrophys. J. Lett.* **896** L32
[63] Regimbau T 2022 The quest for the astrophysical gravitational-wave background with terrestrial detectors *Symmetry* **14** 270
[64] Renzini A I and Golomb J 2024 Projections of the uncertainty on the compact binary population background using popstock *Astron. Astrophys.* **691** A238
[65] Ebersold M, Regimbau T and Christensen N 2024 Next-generation global gravitational-wave detector network: Impact of detector orientation on compact binary coalescence and stochastic gravitational-wave background searches *Phys. Rev. D* **110** 122006
[66] Phinney E S A Practical theorem on gravitational wave backgrounds (arXiv:astro-ph/0108028)
[67] ET 10km noise curve (available at: https://apps.et-gw.eu/tds/?r = 18213)
[68] ET 15km noise curve (available at: https://apps.et-gw.eu/tds/?r = 18213)
[69] CE 40km noise curve (available at: https://dcc.cosmicexplorer.org/CE-T2000017-v7)
[70] A+ noise curve (available at: https://dcc.cosmicexplorer.org/public/0163/T2000007/005/)
[71] A# noise curve (available at: https://dcc.ligo.org/LIGO-T2300041)
[72] Mancarella M, Iacovelli F and Gerosa D 2023 Inferring, not just detecting: metrics for high-redshift sources observed with third-generation gravitational-wave detectors *Phys. Rev. D* **107** L101302
[73] Ng K K Y, Franciolini G, Berti E, Pani P, Riotto A and Vitale S 2022 Constraining high-redshift stellar-mass primordial black holes with next-generation ground-based gravitational-wave detectors *Astrophys. J. Lett.* **933** L41
[74] Stasenko V 2024 Redshift evolution of primordial black hole merger rate *Phys. Rev. D* **109** 123546
[75] Allen B and Romano J D 1999 Detecting a stochastic background of gravitational radiation: signal processing strategies and sensitivities *Phys. Rev. D* **59** 102001
[76] Renzini A I *et al* 2023 pygwb: a python-based library for gravitational-wave background searches *Astrophys. J.* **952** 25
[77] Muratore M, Hartwig O, Vetrugno D, Vitale S and Weber W J 2023 Effectiveness of null time-delay interferometry channels as instrument noise monitors in LISA *Phys. Rev. D* **107** 082004

[78] Regimbau T, Evans M, Christensen N, Katsavounidis E, Sathyaprakash B and Vitale S 2017 Digging deeper: observing primordial gravitational waves below the binary black hole produced stochastic background *Phys. Rev. Lett.* **118** 151105
[79] Sachdev S, Regimbau T and Sathyaprakash B S 2020 Subtracting compact binary foreground sources to reveal primordial gravitational-wave backgrounds *Phys. Rev. D* **102** 024051
[80] Biscoveanu S, Talbot C, Thrane E and Smith R 2020 Measuring the primordial gravitational-wave background in the presence of astrophysical foregrounds *Phys. Rev. Lett.* **125** 241101
[81] Zhou B *et al* Compact binary foreground subtraction in next-generation ground-based observatories (arXiv:2209.01221)
[82] Zhou B *et al* 2023 Subtracting compact binary foregrounds to search for subdominant gravitational-wave backgrounds in next-generation ground-based observatories *Phys. Rev. D* **108** 064040
[83] Zhong H, Zhou B, Reali L, Berti E and Mandic V 2024 Searching for cosmological stochastic backgrounds by notching out resolvable compact binary foregrounds with next-generation gravitational-wave detectors *Phys. Rev. D* **110** 064047
[84] Belgacem E, Iacovelli F, Maggiore M, Mancarella M and Muttoni N 2025 Confusion noise from astrophysical backgrounds at third-generation gravitational-wave detector networks *Phys. Rev. D* **112** 083007
[85] Zhong H, Reali L, Zhou B, Berti E and Mandic V 2025 Two-step procedure to detect cosmological gravitational wave backgrounds with next-generation terrestrial gravitational-wave detectors *Phys. Rev. Lett.* **135** 111401
[86] Giarda G, Renzini A I, Pacilio C and Gerosa D 2025 Accelerated inference of binary black-hole populations from the stochastic gravitational-wave background *Class. Quantum Grav.* **42** 195015
[87] Bhagwat S, Pacilio C, Pani P and Mapelli M 2023 Landscape of stellar-mass black-hole spectroscopy with third-generation gravitational-wave detectors *Phys. Rev. D* **108** 043019
[88] Berti E *et al* Black hole spectroscopy: from theory to experiment (arXiv:2505.23895)
[89] Loffredo E *et al* 2025 Prospects for optical detections from binary neutron star mergers with the next-generation multi-messenger observatories *Astron. Astrophys.* **697** A36
[90] Maggiore M, Iacovelli F, Belgacem E, Mancarella M and Muttoni N 2025 Comparison of global networks of third-generation gravitational-wave detectors *Class. Quantum Grav.* **42** 215004